1 **Seismicity and thermal structure of the St. Paul Transform System, equatorial Atlantic: Insights**
2 **from focal depth analysis**

3

4 Guilherme W. S. de Melo[1], Ingo Grevemeyer[1], Sibiao Liu[1], Marcia Maia[2], Lars Rüpke[1]

5 [1]GEOMAR Helmholtz Centre of Ocean Research Kiel, Kiel, Germany
6 [2]Geo-Ocean, University of Brest, CNRS, Ifremer, UMR6538, F-29280, Plouzane, France

7

8 *Correspondence to*: Guilherme de Melo (gdemelo@geomar.de)

9

10 **Abstract**
11 The slow-spreading Mid-Atlantic Ridge is segmented and offset by transform faults. Among these, the St.
12 Paul Transform System (SPTS), located in the equatorial Mid-Atlantic Ridge, is a complex multi-fault
13 system with four transform faults (Transform A, B, C, and D) and three intra-transform spreading segments
14 with a cumulated offset of 630 km. The SPTS is seismically active, with strong strike-slip earthquakes
15 reaching moment magnitudes of 6.9. In this study, we have re-analyzed the focal depth of 35 earthquakes of
16 the Global Centroid Moment Tensor (GCMT) catalog with $5.3 \leq Mw \leq 6.9$ occurring at Transform A, B, and C
17 since 2004, using regional surface waveform modelling. In addition, we derived a 3-dimensional half-space
18 cooling thermal structure along the transform system that relates the focal depths to the temperature structure.
19 Our results of focal depths indicated that the seismogenic zone of both Transform A, B, and C reaches from
20 5 to 18 km below the seafloor, with the deepest earthquakes located at the center area of the strike-slip
21 segments, and shallower earthquakes occur towards the ridge-transform intersections. The comparison with
22 the half-space cooling indicates that the deepest earthquakes are located in a cooler lithosphere located near
23 the center of the transform segments, with their deformations reaching 600-900ºC. These observations
24 challenge previous viscoplastic mantle geodynamic models that indicated a warm temperature toward the
25 center of a transform fault. The main features found at the SPTS are supported by previous studies of focal
26 depth in other transform faults in the Atlantic Ocean, supporting a global pattern and the occurrence of a
27 cooler mantle at the center of the oceanic transform faults.

28

29 **Short summary**
30 The St. Paul Transform System on the equatorial Mid-Atlantic Ridge is a seismically active multi-fault
31 system. This study re-examines the focal depths of 35 earthquakes (Mw 5.3-6.9) from Transforms A, B, and
32 C. The data suggest that the seismogenic zone ranges from 5 to 18 km deep, with the deepest occurring in
33 cooler lithosphere around the center of the transform segments. This challenges earlier hypotheses and
34 indicates a global pattern of cooler mantle in center of oceanic transform faults.

35

1. Introduction

Transform faults in the equatorial Atlantic Ocean are among the largest and most complex in the world's oceans (e.g., *Bonatti 1990*). Among them, the St. Paul Transform System (SPTS) is a prominent multi-fault transform zone composed of four transform faults (Figure 1) separated by short ridge segments. The SPTS is seismically active, as evidenced by the high frequency of recorded events in seismological catalogs (*Francis et al. 1978; Wolfe et al. 1993; de Melo and Do Nascimento 2018; de Melo et al. 2021a; Parnell-Turner et al. 2022*) with moment magnitude reaching up 6.9 cataloged by the Global Centroid Moment Tensor (GCMT, *Ekstrom et al., 2012*), with both strike-slip faulting focal mechanism occurring along the transform fault segments of the SPTS. In addition, some thrust faulting earthquakes were observed in the vicinity of the St. Peter and St. Paul islands in the northernmost transform fault (*Wolfe et al. 1993*). Unfortunately, GCMT solutions are subject to considerable epicentral uncertainties that can reach ~70 km in distance from the appropriate tectonic features (*Pan et al. 2002*), limiting their reliability in detailed tectonic analyses.

Characterizing the seismicity of oceanic transform faults is critical to understanding the physical properties of the oceanic lithosphere, such as earthquake depths and their distribution along the transform fault segments. Previous seismological studies of focal depth in oceanic transform faults found that the maximum depth of the brittle-ductile transition zone occurs at the center of the transform fault where the cooling is most pronounced, while shallower events are concentrated close to the ridge-transform intersections (*e.g. Bergman and Solomon 1988; Abercrombie and Ekström 2001*). However, it has been suggested that a viscous-plastic rheology approximates the behavior of the oceanic lithosphere best, resulting into warmer temperatures toward the middle of the transform (*Behn 2007; Liu et al., 2023*). For the Blanco transform fault offsetting the intermediate spreading Juan de Fuca Ridge in the NW Pacific Ocean, Roland et al. (2010) showed the numerical simulation introducing a viscous-plastic rheology are able to yield the spatial distribution of earthquakes. Yet, earthquakes along the Blanco transform did not reveal a profound increase of focal depth near the center of the transform segments (*Ren et al. 2023*) as found for transform faults in the Atlantic Ocean (*Bergman and Solomon 1988*).

62   In this paper, we report the focal depth of 35 earthquakes of the SPTS cataloged by the GCMT with

63   Mw=>5.3, using regional seismic stations at the equatorial Atlantic. We use regional waveform modelling

64   of surface waves to relocate epicenters onto the appropriate surface trace of transform imaged in bathymetric

65   data (*Maia et al. 2016*). In addition, the procedure yields focal depth, and we observe that deeper earthquakes

66   are located mostly in the middle of the transform segments of the SPTS and centroids occur at temperatures

67   of 600 to 900ºC. Therefore, our results of the focal depth solutions suggest that oceanic transform faults

68   generally present deeper earthquakes toward their central and cooler domains.

2. Study area

70   The St. Paul Transform System is a complex multi-transform system composed of four transforms named

71   A, B, C, and D, that offset the axis of the Mid-Atlantic Ridge (MAR) by 303, 142, 88, and 53 km,

72   respectively (*Schilling et al.* 1995; *Maia et al.* 2016). Within this system, three short intra-transform ridge

73   (ITR) segments of the MAR axis have been identified (*Maia et al.* 2016). Transform A is slowly slipping

74   at a rate of 27.71 mm/year (*DeMets et al 2010*). A prominent topographic feature along transform A is the

75   Atobá Ridge, 200 km long and 30 km wide, that reaches the sea level at Saint Peter and Saint Paul

76   Archipelago (SPSPA; 0˚55'N and 29˚38'W) (*Maia et al. 2016*). SPSPA is a set of 6 islets and 4 rocks

77   composed of peridotite mylonite and alkaline ultramafic mantle rocks with different serpentinization

78   degrees (*Melson et al.* 1967, *Hekinian et al.* 2000; *Campos et al. 2022*). Samples obtained from the

79   submarine parts of the Atobá Ridge along the COLEMIA (COLd Mantle Exhumation and Intra-transform

80   Accretion) cruise (*Maia et al.* 2016), either by dredging or by submersible, were also predominately

81   serpentinized mantle rocks (*Hekinian et al.* 2000; *Maia et al.* 2016). *Maia et al.* (2016) constrained the age

82   offset along the transform system (Figure S1) and revealed a low-density layer (LDL; Figure S2) beneath

83   the SPTS, which is interpreted in terms of a layer of serpentinized mantle (limited at 500ºC) as the nature

84   of the rock sampled at the seafloor suggests that the low density layer may represent serpentinized mantle

85   rather than magmatic crust. Transform A is highly segmented and composed of a diversity of restraining

86   bends and stepovers, which induce local transpression in the Atobá Ridge area resulting in the ridge uplift

87   and consequent exhumation of the mantle rocks (*Maia et al.* 2016). The present-day uplift rate is estimated

88   to be 1.5 mm/year (*Campos et al.* 2010). Bickert et al. (2023) showed that the fluid percolation in Transform

89   A causes a grain size reduction and weakens the local fault strength along the eastern part of the Atobá

90   Ridge. To the best of our knowledge, the Atobá Ridge is the largest known example of a push-up ridge in

91   the oceanic lithosphere and the only case studied so far.

92   Transform B extends between the ~27.6˚ and 26.4˚W longitude range and is formed by a principal

93   transform displacement zone (PTDZ) slowly slipping at 27.77 mm/year (*DeMets et al 2010*), with a deep

94   valley reaching more than 5500 m beneath the sea level (bsl) close to the western ridge-transform

95   intersection (RTI) with ~4,000 m bsl in its middle part. Transform C is slipping at 27.83 mm/year (*DeMets*

96   *et al 2010*), extending between the ∼26.3˚ and 25.55˚W longitude range, with a deep valley reaching more

97   than 5000 m bsl. Transform D is the shortest transform, occurring between ∼25.5˚ and 25.05˚ W, with a

98   transform valley reaching approximately 4500 m bsl. Long-lived oceanic core complexes exhuming mantle

99   rocks have been mapped along the segment between Transforms C and D, suggesting colder spreading

100   contexts (*Vincent et al 2023*).

2.1. Seismotectonic of the St. Paul Transform System

102   At Transform A, the local micro-seismicity has been recorded by a local station installed at SPSPA

103   islets (*de Melo and do Nascimento. 2018*), revealing a seismically active setting. Fault plane motions

104   analyzed by the GCMT along the SPTS (Figure 1b; Figure S3) indicate that most of the solutions are strike-

105   slip, consistent with the main transform fault orientations. However, at Transform A, some solutions differ

106   from the expected transform fault kinematics, confirming complex fault geometry and segmentation.

107   Previous studies reported compressive mechanisms, uncommon for transform fault areas, near the SPSPA

108   islets in Transform A (e.g. *Wolfe et al. 1993*). Wolfe et al (1993) identified focal depths reaching up to 14

109   km below seafloor (bsf) in earthquakes that occurred at Transform A, while Engeln et al. (1986) found in

110   strike-slip solutions with a focal depth of 3-7 km bsf at the same transform segment. Francis et al (1978)

111   reported microseismicity with focal depth reaching up to 11 km bsf at Transform D. Wolfe et al. (1993)

112   suggested that additional factors may control the occurrence of compressive earthquakes in Transform A,

113   such as recent changes in plate motion, differential lithospheric cooling, or the development of a weakened

114   fault zone. More recently, Maia et al. (2016) favored a southward propagation of the MAR into the transform

115   domain as a possible mechanism generating the large stepovers and associated thrust faults.

3. Data acquisition

118   In this work, we use 35 regional earthquakes with moment magnitude (M_W)>5.3 reported by the

119   GCMT since 2004 over transforms A, B, and C. No earthquakes with M_W>5.3 were cataloged in transform

120   D over the same time. The dataset includes permanent 3-component broad brand seismometers belonging to

121   the Brazilian Seismographic Network (RSBR, *Bianchi et al.* 2018), the IRIS/IDA (Incorporated Research

122   Institutions for Seismology) network (Scripps Institution of Oceanography, 1986), and GEOSCOPE

123   (doi:10.18715/GEOSCOPE.G). These networks were chosen based on the epicentral distance to the

124   earthquakes and the data availability (see histogram in Figure 1a). In addition, we also included data from

125   temporary stations installed by the BLSP2002 project (*Feng et al.* 2004) in North-Northeast Brazil to analyze

126   earthquakes that happened in 2004-2005.

4. Methodology

4.1. Surface Waveform Modeling

129   We study the epicentral location and focal depth of the 35 earthquakes using a surface waveform

130 model from records of 21 regional seismic stations at 1,000-3,050 km distance range (Figure 1a; Table S1;

131 Figure S4). We only use stations where the Rayleigh waves present a good signal-to-noise ratio after

132 filtering by a low-frequency filter (0.02-0.04 Hz). The waveform modeling was performed using an open-

133 source MATLAB code package called ISOLA (*Sokos and Zahradnik* 2008; *Zahradnık and Sokos* 2018).

134 The regional earthquakes used for modeling were chosen in the GCMT catalog based on two criteria: 1 –

135 Data availability in networks; 2 – A magnitude threshold of M_W 5.3, which from our experience (*de Melo*

136 *et al 2021; 2024*), provides signals with sufficiently high signal-to-noise ratio suitable for surface waveform

137 model. All epicenter-station ray paths are represented in Figure 1a, with the operation time of the stations.

138 A simple 1D crustal velocity model obtained from the CRUST1.0 global model (*Laske et al.* 2013)

139 was used on ISOLA to model the surface waves in the oceanic crust. The model process starts with applying

140 a 4th-degree Butterworth filter to remove the instrumental response and generate displacement waveforms

141 in the frequency range of 0.02-0.04 Hz frequency range. In some cases, we modified the filter frequency

142 range to 0.01-0.03 Hz for the farthest stations (e.g. DBIC and MPG; see Figure 1a). Next, a synthetic

143 displacement waveform is generated for comparison, using the same filter frequency applied station by

144 station. Green's functions were calculated using the AXITRA program (*Coutant* 1989), implemented in the

145 ISOLA package. We used the fixed point-source ISOLA inversion, which fixes the strike/dip/range angles,

146 applying focal mechanism angles provided by the GCMT catalog (*Dziewonski et al.* 1981; *Ekstrom et al.*

147 2012). ISOLA searches for the best solution across a grid e of sources spaced at 1 km intervals.

148 Large strike-slip earthquakes should rupture along the PTDZ (*de Melo et al 2025*). Instead, we

149 observed that the location of the GCMT epicenters are biased and occur sometimes several tens of

150 kilometers away from the transform valley at Transform B and C (Figure S3). Pan and Dziewonski (2005)

151 found that GCMT epicenters can be located up to half a degree from the proper tectonic plate borders.

152 Therefore, we modified the epicentral coordinates, keeping the GCMT longitude, but moving the latitude

153 onto the PTDZ mapped in multibeam data (*Maia et al 2016*). The distance between GCMT epicenter and

154 the new modified epicenter vary from 0.44 to 20 km with average of 11.25 km (Figure 2).

155 Recorded/synthetic waveform best-fitting solutions are described by the focal depth, centroid-time (CT),

156 seismic moment (M_0), moment magnitude (M_W), CN (condition number which tells us whether the inversion

157 problem is ill-posed, values below 5 indicate the moment-tensor which is relatively well resolved), the

158 double-couple percentage (DC) and 95% confidence interval VR (1). We estimate the depth uncertainties

159 using a computer code that expands the ISOLA package solutions (*Dias et al.* 2016), which applies several

160 different frequency ranges in the waveform inversion to reveal the stability and uncertainty of the solution

161 of the aforementioned centroid parameters considering a threshold (0.95) concerning the solution with the

162 largest VR. Three waveform-fitting examples of earthquakes with Mw 6.9, 5.9 and 5.7 are shown in Figure

163   3-5. We used 4-10 stations during the analysis (Figure 6a; Table S2), depending on the data availability.

164   The mean 95% confidence interval for the earthquake waveform fitting shows VRs from 0.41 to 0.69, with

165   most vertical components often exceeding 0.90 (Figure 6b; Table S2). Most CN solutions of the earthquakes

166   are <4.5 (Figure 6c; Table.S2), with the CTs obtained in analysis ranging from -0.2 to 4.8 s (Figure 6d;

167   Table.S2). Changes in parameters like source-station orientation and velocity model provide new ISOLA

168   solutions with higher VR values. We used regional distance records, which makes it difficult to find an

169   adequate single velocity model to provide results with VRs close to 1.0 for all components (*de Melo et al*

170   *2021; 2024*). Nevertheless, low values of VR do not necessarily signify that a solution is ill-posed once

171   ISOLA considers fitted solutions with VR of 0.4 or more (*Zahradnık and Sokos* 2018).

172

173   4.2. Thermal Structure Modeling

174   We employ the approach of the classical half-space cooling model to construct the thermal structure

175   of the SPTS. A geodynamic model can be found in Text S1 and Figure S5. The temperature field in the

176   cooling model is derived from the oceanic plate temperature formula (*Turcotte and Schubert 2014*):

177
$$T = T_s + (T_m - T_s)\left(1 - erfc\left(\frac{z}{2\sqrt{\kappa x/u}}\right)\right)$$

178   where T_s (0 °C) and T_m are temperatures of the surface and mantle, respectively, z is the depth from 0 at the

179   seafloor down to 200 km, κ is the thermal diffusivity (10^{-6} m^2/yr), x is the distance from the ridge axis, and

180   u is the spreading rate (27.8 mm/year; *DeMets et al 2010*). Previous studies reported that the mantle

181   temperature in the equatorial Atlantic might be ~150ºC lower than elsewhere in the Atlantic Ocean (*Bonatti*

182   *1990; Bonatti et al. 1993; Schilling et al .1995; Hékinian et al. 2000; Le Voyer et al. 2015*). Consequently,

183   we tested two different potential mantle temperatures of 1150 and 1300°C. To account for thermal

184   transitions across transform offsets, the temperature field beneath each transform segment is modified by

185   averaging the temperatures of the adjacent ridge segments on both sides.

186   To evaluate the impact of different thermal structures, we extracted the depths of the 500°C, 600°C,

187   and 900°C isotherms from both models across three transform segments (A, B, and C). The comparison

188   between the two mantle temperature scenarios reveals significant spatial variations. Transform A exhibits

189   systematically shallower isotherms in areas away from the ridge in the 1300°C model (Figure 7a), indicating

190   a hotter lithosphere compared to the central region of the transform fault segment. In Transform B and C

191   (Figure 7b,c), the 500°C and 600°C isotherms show minimal differences, whereas the 900°C isotherm given

192   by the 1300°C model is notably shallower than Transform A due to the shorter offset area.

5. Results

The 35 events analyzed in Transforms A, B, and C focal show depths between 5±4 and 18±2 km bsf (Figure 8; Table S2). At Transform A, the magnitude of the 20 events ranges from 5.3 to 6.5 M_W. The focal depths vary between 5±3 km and 18±2 km bsf. Just two events were found in its western area of the Transform A, rupturing between 30.5° and 29.8° W longitudes, with the two epicenters of Mw 6.3 and 6.5 located close to each other, and focal depths at 9±3 and 10±5 km bsf, with an average of 9.5 km. Nine earthquakes are located beneath the Atobá Ridge between 29.6-28.6°W longitude, with focal depths ranging from 9±2 to 18±2 km bsf and an average of 14.3 km, most of them situated in the ridge flanks, close to the mapped thrust faults. At the eastern area of Transform A between 28.5 to 27.75°W longitudes, eight strike-slip earthquakes presented focal depths with an average of 9.4 km, ranging from 6±4 to 14±2 km bsf, and their epicenters located in a deep basin crossed by the PTDZ. The zone is more linear and less segmented than the west and central areas of Transform A (*Maia et al.* 2016). Five events with moment magnitudes ranging from M_W 5.3-6.9 were analyzed for Transform B, providing an average of 7.8 km bsf. Two of the strike-slip earthquakes occur in the middle of the segment, with focal depths of 10±4 and 9±4 km bsf. The other two events are in the east zone close to the spreading segment separating the Transforms B and C, with focal depths of 6±3 km bsf for both earthquakes. Eight focal depth estimates are available for Transform C, with an average of 7.4 km bsf. The best-fitting waveforms show results with a 5-11 km depth range and a maximum uncertainty of 4 km, with most epicenters located over the restraining bends.

In general, our results from waveform modeling of the 35 earthquakes shows that the thickness of the seismogenic zone varies along the three transform segments (A, B, and C), with a maximum focal depth of 18 km. Wolfe et al. (1993) previously analyzed six earthquakes at Transform A, revealing focal depths of 8-14 km bsf. Our depth estimates are at least 3.5 km shallower than the depth reported in the GCMT catalog (Figure 7), which its common since GCMT does not consider the water layer in the depth analysis (*Ekström et al.* 2012). In our case, we assume the depth already removing the 5.1 km water layer of the CRUST1.0 (see *de Melo et al. 2021*). Just one earthquake that occurred in 2004-10-25 displayed focal depth deeper than those of the GCMT, which can be due to the poor seismographic network coverage during that period (Figure 1).

221

6. Discussion

6.1. Epicenter Distribution along the Transform Faults

Oceanic transform faults undergo significant water percolation, thus inducing mantle rocks alteration (*Bonatti* 1976; *Francis et al.* 1978; *Detrick et al.* 1993; *Roland et al.* 2010). Serpentinization consistently reduces the bulk density and influences the strength and the tectonic style of the slow-spreading oceanic lithosphere (*Escartin et al.* 1997; *Escartin et al.* 2001). Bickert et al. (2023), for example, demonstrated that fluid-rock interactions take place under the Atoba Ridge, altering the rheology at Transform A. These effects govern the deformation and subsequently the fault activity in the Transform A region. Recent studies have used teleseismic relative relocation to compare the earthquake distribution along globally oceanic transform faults, indicating that ~68% of the SPTS area will behaves aseismically (*Shi et al 2021*). However, the author did not consider the transform segmentation along the transform fault system neither comparison with local structure features presented by high resolution bathymetry.

We compared the new location of the earthquakes with the local structure presented by the multibeam data at Transform B and C. At Transform B, the five epicenters cover the PTDZ from its eastern RTI towards the center, indicating that a total of ~45% of the PTDZ is seismically active. Although we are using only five earthquakes, the same seismic coupling proportion apply compared to the entire GCMT catalog since 1990 (Figure S3). However, that proportion increase compared to nine earthquakes analyzed at Transform C, with the PTDZ seismically active for ~75% of the whole PTDZ extension. Additionally, the active area of the Transform C can increase to ~80% if we consider the whole GCMT catalog. So, these features indicate that at least ~45% of the Transform B and ~75-80% of the Transform C extension are seismically active, contradicting the aseismic proportion provided by previous results (*Shi et al 2021*). Locals features such as a cold upper mantle could explain a different strength along the Transform A and B.

6.2. The focal depth distribution along the transform faults

The maximum depth of seismic faulting is controlled by the brittle to ductile transition which is itself a function of temperature. Early studies suggested that earthquakes along Atlantic transforms occur at shallow depth of ~4 km with no events occurring deeper than 7 km (*Engeln et al., 1986*). However, waveform inversion for focal mechanisms and focal depth, mostly based on teleseismic recordings, showed that these very shallow focal depths and little depth variation along a transform fault might not be correct.

253   Instead, focal depth my vary profoundly along oceanic transform faults, with shallower earthquake

254   occurrence near ridge-transform intersections and deeper earthquakes in the center of segments. For

255   example, Bergman and Solomon (1988) found that at the Charlie-Gibbs and Vema transform faults focal

256   depths increase towards the center, deepening from 4-5 km near transform-ridge intersections (RTI) and

257   reaching a maximum depths of 14-20 km bsf in the center of the transforms. Similar patterns are found by

258   Fang and Abercrombie (2023) at the Chain transform in the equatorial Atlantic, revealing that earthquakes

259   ruptured at~20-25 km near its center, while the shallower earthquakes clustered at 5-10 km near the RTIs.

260   Abercrombie and Ekström (2001) also observed for the Chain transform focal depths of ~8-10 km near the

261   RTI and ~12-16 km depth for earthquakes occurring away from both RTIs. At the Romanche transform,

262   the longest transform fault in the equatorial Atlantic, they found identical pattern, though focal depth

263   reached with 8-12 km and ~12-21 km somewhat deeper into the lithosphere at both RTIs and near its center,

264   respectively.

265   The focal depths examined in our study are based on regional waveforms instead of teleseismic data

266   and range from 5 to 18 km bsf along the transforms A, B, and C of the St. Paul transform system. At

267   Transform A, earthquakes in its central area and beneath the Atoba Ridge reach 9-18 km bsf, earthquakes

268   closest to the western RTI reach 9-10 km bsf, and earthquakes near to the eastern RTI have a focal depth

269   of 5-14 km bsf (Figure 8). We see focal depths of earthquakes ranging from 6 to 10 kilometers along

270   Transform B, with the deeper ones situated in the center (Figure 8). Earthquakes at Transform C display

271   focal depths 5-11 km beneath the seafloor (Figure 8). Therefore, our observations, in concert with previous

272   investigations from teleseismic data (e.g., *Bergman and Solomon, 1988; Abercrombie and Ekström, 2001;*

273   *Fang and Abercrombie, 2023*), provide a comprehensive understanding of how focal depths are distributed

274   along transform faults revealing a systematic change of focal depths with deeper earthquakes occurring in

275   the central area of transforms and shallow events near the RTIs.

276

277   6.3. Focal depth and thermal structure

278   Early seismic studies of oceanic transform faults found rather shallow focal depth, suggesting that

279   earthquakes may occur at a similar thermal range (50-300°C) as those along continental faults (*Burr and*

280   *Solomon, 1978*). The distribution of seismicity along both Chain and Romanche transform faults matches

281   plate cooling thermal models, demonstrating the importance of temperature in determining focal depth and

282   suggesting that most earthquakes occur with maximum depth until the 600°C isotherm (*Abercrombie and*

283   *Ekström 2001*). However, other studies suggested that some earthquakes may rupture at a higher

284 temperature. For example, Bergman and Solomon (1988) suggested from their thermal models that
285 seismicity is limited to the thickness of the lithosphere (~900°C isotherm).

286   Morgan and Forsyth (1988) developed a 3-dimmensional numerical model to explain seismicity
287 patterns in the mid-ocean ridge system with transform offsets, including the increase in earthquake
288 occurrence away from the RTIs towards the transform center. Their model, however, introduces an
289 isoviscous rheology, whereas modern geodynamic model studies favor nonlinear viscoplastic rheology,
290 which provides a better approximation of the mantle dynamics (*Behn et al., 2007; Liu et al., 2023*).
291 However, these models predict a strain localization that causes warm mantle upwelling beneath the
292 transform fault, which contradicts observations of deeper seismicity toward transform centers. One
293 potential explanation might be that active hydrothermal circulation along transform faults may dissipate
294 heat at their centers. Nevertheless, without independent evidence for the amount of hydrothermal mining
295 of heat, we instead use a 3-dimensional half-space cooling model to study the relationship between thermal
296 state and seismogenesis.

297   Our thermal model considers two thermal scenarios: a standard mantle temperature of 1300ºC
298 commonly used in the literature and a colder mantle (1150ºC) based on previous studies indicating a lower
299 mantle temperature in the equatorial Atlantic (*Bonatti 1990; Bonatti et al. 1993; Schilling et al .1995;*
300 *Hékinian et al. 2000; Le Voyer et al. 2015*). The model results show that the depth of the 600°C isotherm,
301 corresponding to the maximum depth of the brittle deformation (*Abercrombie and Ekström* 2001), increase
302 with transform offset length (Figure 9a,b). Transform A present the maximum depths, ~11 and 13 km bsf,
303 for 1300ºC and 1150ºC models, respectively (Figure 8). At Transform B, the 600°C isotherm is located at
304 depths of 7.9 and 9 km, and at Transform C, the isotherm reaches 6 and 7 km (Figure 8). For both thermal
305 scenarios, the deeper earthquakes are located above isotherms of 780-880ºC at the center of the Transform
306 A, 660-750ºC in Transform B, and 850-960ºC in Transform C. Across all transforms, the depth of the
307 earthquakes increases with the modelled mantle temperature (Figure 9bc). Similarly, recent examinations
308 of focal depths using Ocean-Bottom seismometer data along the Chain transform fault revealed that the
309 seismogenic zone is deeper than the fault's maximum predicted depths in the center (*Leptokaropoulos et al.*
310 *2023; Schlaphorst et al. 2023*). These results suggest that the focal depth distribution compared with model
311 temperatures indicate that the seismic deformation occur inside a general range from ~600 to 900ºC along
312 the length of the fault, reinforcing the idea that the center of transform faults is cooler than RTIs. In addition,
313 the half-space results assuming a colder mantle temperature (1150ºC) fits better with observed focal depths
314 (Figure 8).

315   Our results suggest that the depth of seismogenic zone beneath transforms A, B, and C agree with

316   expected maximum deformation presented by previous structural, geochemical, and seismological analyses

317   (*Wolfe et al 1993; Roland et al. 2010; Barão et al 2020; Prigent et al. 2020; Bickert et al. 2023*). However,

318   these results challenge the brittle weakening with viscoplastic mantle rheology done by Behn et al (2007),

319   in which predicted warmer temperatures toward the middle of the transform caused by mantle upwelling

320   and cooling toward the ridge segments (*Behn et al. 2007*). Instead, our observations support a cooler

321   transform center, potentially influenced by hydrothermal activity and lower ambient mantle temperatures

322   in the equatorial Atlantic.

323

324

325   **Conclusion**

326   We relocated earthquakes along the St. Paul transform fault system to the active fault using regional

327   waveform modelling of surface waves and bathymetric data. From our analysis of focal depths and thermal

328   modelling we conclude that

329

330   1.The strike-slip segments of the SPTS are strongly segments revealing a considerable variation in seismic

331   coupling, showing that between 45-80% of the mapped fault are seismically active.

332

333   2.The horizontal distribution of focal depths along Transforms A, B, and C reveals that the epicenters of

334   the deepest earthquakes occur near the center zone of the PTDZs, whereas shallower focal depths are found

335   near RTIs. These findings indicate that the horizontal distribution of seismic behavior at the St. Paul

336   transform system is consistent with previous studies conducted on other transform faults such as Charlie-

337   Gibbs, Vema, Romanche, and Chain.

338

339   3-Compared with the thermal model, the deepest earthquakes at the center zone of Transforms A, B, and

340   C, are in colder area with lower temperatures along the PTDZ. Furthermore, the shallower earthquakes

341   hotter areas close to the RTI. These results support the existence of a colder upper mantle at center of the

342   oceanic transform faults, challenging features issued by viscoplastic mantle rheology models.

343

344

345

Acknowledgments

GWSdM was funded by the European Union through MSCA-DN-ENVSEIS-101073148, and IG by ERC-TRANSFORMERS-101096190. GWSdM thanks for rich comments and tips of Jiri Zahradnik about the surface waveform modeling, and Fabio Dias for provides the code to the uncertainty's calculation. We acknowledge the Resource Allocation Board, Germany for providing computational resources. Computations of thermal models in this study were performed on the supercomputers at NHR@ZIB under the projects SHK00051 and BBP00064. Thank captain Gilles Ferrand and his crew and the COLMEIA scientific party for their help during the COLMEIA cruise. Funding COLMEIA ship time was funded by the grant to the Flotte océanographique française. Financial support for the cruise and preliminary data processing came from CNRS INSU Campagnes à la Mer and Labex Mer.

Data Availability Statement

The broadband seismic waveform data of the Brazilian Seismographic Network (RSBR; Bianchi et al. 2018) network can be obtained at http://rsbr.on.br/request.html. The seismic data of the BLSP2002 project (*Feng et al 2004*), the GEOSCOPE network (*Romanowicz et al 1984*), and other global stations were downloaded by EarthScope Consortium Inc (*https://service.iris.edu/*). The ISOLA package (*http://seismo.geology.upatras.gr/isola/*) is applied for data processing and waveform models using MATLAB version 9.6 (*The MathWorks Inc. 2019*). The Global Centroid Moment Tensor database (*http://www.globalcmt.org*) was last accessed in March 2025. Maps and graphics were made with Generic Mapping Tools, version 6.6.0 (*Wessel et al.* 2019). Bathymetric data in Figure 1 was based on the Global Multi-Resolution Topography (GMRT; *Ryan et al. 2009*), version 4.3, available at https://www.gmrt.org/GMRTMapTool/, and accessed in February 2025. Additional Supplement Material information about the analysis for all earthquakes is accessible using the Zenodo repository (*de Melo et al. 2025*).

Author contribution

GWSM conducted the conceptualization, data curation, methodology and formal analysis of the waveform modeling, investigation, and validation of the focal depths. IG and MM contributed with supervision. SL developed the methodology, formal analysis, and validation of the thermal modeling. GWSdM, IG, SL, and MM contributed to the interpretation of the results. IG and LR provided funding acquisition and resources. GWSdM wrote the manuscript with contributions and reviews from all co-authors.

Competing interests.

The contact author has declared that none of the authors has any competing interests.

References

Abercrombie, R. E., & Ekström, G. (2001). Earthquake slip on oceanic transform faults. *Nature*, *410*(6824), 74-77. https://doi.org/10.1038/35065064

Barão, L. M., Trzaskos, B., Angulo, R. J., & de Souza, M. C. (2020). Deformation and structural evolution of mantle peridotites during exhumation on transform faults: A forced transition from ductile to brittle regime. *Journal of Structural Geology*, *133*, 103981. https://doi.org/10.1016/j.jsg.2020.103981

Behn, M. D., Boettcher, M. S., & Hirth, G. (2007). Thermal structure of oceanic transform faults. *Geology*, *35*(4), 307-310. https://doi.org/10.1130/G23112A.1

Bergman, E. A., & Solomon, S. C. (1988). Transform fault earthquakes in the North Atlantic: Source mechanisms and depth of faulting. *Journal of Geophysical Research: Solid Earth*, *93*(B8), 9027-9057. https://doi.org/10.1029/JB093iB08p09027

Bianchi, M. B., Assumpção, M., Rocha, M. P., Carvalho, J. M., Azevedo, P. A., Fontes, S. L., ... & Costa, I. S. (2018). The Brazilian seismographic network (RSBR): improving seismic monitoring in Brazil. *Seismological Research Letters*, *89*(2A), 452-457. https://doi.org/10.1785/0220170227

Bickert, M., Kaczmarek, M. A., Brunelli, D., Maia, M., Campos, T. F., & Sichel, S. E. (2023). Fluid-assisted grain size reduction leads to strain localization in oceanic transform faults. *Nature Communications*, *14*(1), 4087. https://doi.org/10.1038/s41467-023-39556-5

Bonatti, E. (1976). Serpentinite protrusions in the oceanic crust. *Earth and Planetary Science Letters*, *32*(2), 107-113. https://doi.org/10.1016/0012-821X(76)90048-0

Bonatti, E. (1990). Subcontinental mantle exposed in the Atlantic Ocean on St Peter–Paul islets. *Nature*, *345*(6278), 800-802. https://doi.org/10.1038/345800a0

Bonatti, E., Seyler, M., & Sushevskaya, N. (1993). A cold suboceanic mantle belt at the Earth's equator. *Science*, *261*(5119), 315-320. https://doi.org/10.1126/science.261.5119.315

Burr, N. C., & Solomon, S. C. (1978). The relationship of source parameters of oceanic transform earthquakes to plate velocity and transform length. *Journal of Geophysical Research: Solid Earth*, *83*(B3), 1193-1205. https://doi.org/10.1029/JB083iB03p01193

Campos, T. F., Bezerra, F. H., Srivastava, N. K., Vieira, M. M., & Vita-Finzi, C. (2010). Holocene tectonic uplift of the St Peter and St Paul Rocks (Equatorial Atlantic) consistent with emplacement by extrusion. *Marine Geology*, *271*(1-2), 177-186. https://doi.org/10.1016/j.margeo.2010.02.013

Campos, T. F., Sichel, S. E., Maia, M., Brunelli, D., Motoki, K., Magini, C., ... & de Melo, G. (2022). The singular St. Peter and St. Paul Archipelago, equatorial Atlantic, Brazil. In *Meso-Cenozoic Brazilian Offshore Magmatism* (pp. 121-165). Academic Press. https://doi.org/10.1016/B978-0-12-823988-9.00003-4

Coutant, O. (1989). Program of numerical simulation AXITRA. *Res. Rep. LGIT (in French), Universite Joseph Fourier, Grenoble*.

DeMets, C., Gordon, R. G., & Argus, D. F. (2010). Geologically current plate motions. *Geophysical journal international*, *181*(1), 1-80. https://doi.org/10.1111/j.1365-246X.2009.04491.x

de Melo, G. W. S., & Do Nascimento, A. F. (2018). Earthquake magnitude relationships for the Saint Peter and Saint Paul archipelago, equatorial atlantic. *Pure and Applied Geophysics*, *175*, 741-756. https://doi.org/10.1007/s00024-017-1732-6

de Melo, G. W. S., Mitchell, N. C., Zahradnik, J., Dias, F., & do Nascimento, A. F. (2021). Oceanic seismotectonics from regional earthquake recordings: the 4–5° N mid-Atlantic ridge. *Tectonophysics*, *819*, 229063. https://doi.org/10.1016/j.tecto.2021.229063

de Melo, G. W. S., Mitchell, N. C., & Sokolov, S. Y. (2024). The 2020 Mw 6.6 Vernadsky transform earthquake sequence: rupture and Coulomb stress changes surrounding an oceanic core complex. *Marine Geophysical Research*, *45*(4), 28. https://doi.org/10.1007/s11001-024-09558-z

de Melo, G. W. S., Grevemeyer, I., Lange, D., Metz, D., & Kopp, H. (2025). Relationship between rupture length and magnitude of oceanic transform fault earthquakes. *Geophysical Research Letters*, *52*(1), e2024GL112891. https://doi.org/10.1029/2024GL112891

de Melo, G. W. S., Grevemeyer, I., Liu, S., Maia, M., & Ruepke, L. (2025). Seismicity and thermal structure of the St. Paul Transform System, equatorial Atlantic: Insights from focal depth analysis [Dataset]. *Zenodo*. https://doi.org/10.5281/zenodo.15204422

Detrick, R. S., White, R. S., & Purdy, G. M. (1993). Crustal structure of North Atlantic fracture zones. *Reviews of Geophysics*, *31*(4), 439-458. https://doi.org/10.1029/93RG01952

Dias, F., Zahradník, J., & Assumpção, M. (2016). Path-specific, dispersion-based velocity models and moment tensors of moderate events recorded at few distant stations: examples from Brazil and Greece. *Journal of South American Earth Sciences*, *71*, 344-358. https://doi.org/10.1016/j.jsames.2016.07.004

Dziewonski, A. M., Chou, T. A., & Woodhouse, J. H. (1981). Determination of earthquake source parameters from waveform data for studies of global and regional seismicity. *Journal of Geophysical Research: Solid Earth*, *86*(B4), 2825-2852. https://doi.org/10.1029/JB086iB04p02825

Ekström, G., Nettles, M., & Dziewoński, A. M. (2012). The global CMT project 2004–2010: Centroid-moment tensors for 13,017 earthquakes. *Physics of the Earth and Planetary Interiors*, *200*, 1-9. https://doi.org/10.1016/j.pepi.2012.04.002

Engeln, J. F., Wiens, D. A., & Stein, S. (1986). Mechanisms and depths of Atlantic transform earthquakes. *Journal of Geophysical Research: Solid Earth*, *91*(B1), 548-577. https://doi.org/10.1029/JB091iB01p00548

Escartin, J., Hirth, G., & Evans, B. (1997). Effects of serpentinization on the lithospheric strength and the style of normal faulting at slow-spreading ridges. *Earth and Planetary Science Letters*, *151*(3-4), 181-189. https://doi.org/10.1016/S0012-821X(97)81847-X

Escartin, J., Hirth, G., & Evans, B. (2001). Strength of slightly serpentinized peridotites: Implications for the tectonics of oceanic lithosphere. *Geology*, *29*(11), 1023-1026. https://doi.org/10.1130/0091-7613(2001)029%3C1023:SOSSPI%3E2.0.CO;2

Fang, H., & Abercrombie, R. E. (2023). SMatStack to enhance noisy teleseismic seismic phases: Validation and application to resolving depths of oceanic transform earthquakes. *Geochemistry, Geophysics, Geosystems*, *24*(11), e2023GC011109. https://doi.org/10.1029/2023GC011109

Feng, M., Assumpçao, M., & Van der Lee, S. (2004). Group-velocity tomography and lithospheric S-velocity structure of the South American continent. *Physics of the Earth and Planetary Interiors*, *147*(4), 315-331.

478   https://doi.org/10.1016/j.pepi.2004.07.008
479
480   Francis, T. J. G., Porter, I. T., & Lilwall, R. C. (1978). Microearthquakes near the eastern end of St Paul's Fracture
481   Zone. *Geophysical Journal International*, *53*(2), 201-217. https://doi.org/10.1111/j.1365-246X.1978.tb03738.x
482
483   Hekinian, R., Juteau, T., Gracia, E., Sichler, B., Sichel, S., Udintsev, G., ... & Ligi, M. (2000). Submersible
484   observations of equatorial atlantic mantle: the St. Paul Fracture Zone region. *Marine Geophysical Researches*, *21*,
485   529-560. https://doi.org/10.1023/A:1004819701870
486
487   Laske, G., Masters, G., Ma, Z., & Pasyanos, M. (2013, April). Update on CRUST1. 0—A 1-degree global model of
488   Earth's crust. In *Geophysical research abstracts* (Vol. 15, No. 15, p. 2658).
489
490   Le Voyer, M., Cottrell, E., Kelley, K. A., Brounce, M., & Hauri, E. H. (2015). The effect of primary versus
491   secondary processes on the volatile content of MORB glasses: An example from the equatorial Mid-Atlantic Ridge
492   (5 N–3 S). *Journal of Geophysical Research: Solid Earth*, *120*(1), 125-144. https://doi.org/10.1002/2014JB011160
493
494   Leptokaropoulos, K., Rychert, C. A., Harmon, N., Schlaphorst, D., Grevemeyer, I., Kendall, J. M., & Singh, S. C.
495   (2023). Broad fault zones enable deep fluid transport and limit earthquake magnitudes. *Nature
496   Communications*, *14*(1), 5748. https://doi.org/10.1038/s41467-023-41403-6
497
498   Liu, S., Guo, Z., Rüpke, L. H., Morgan, J. P., Grevemeyer, I., Ren, Y., & Li, C. (2023). Sensitivity of gravity
499   anomalies to mantle rheology at mid-ocean ridge–transform fault systems. *Earth and Planetary Science
500   Letters*, *622*, 118420. https://doi.org/10.1016/j.epsl.2023.118420
501
502   Maia, M., Sichel, S., Briais, A., Brunelli, D., Ligi, M., Ferreira, N., ... & Oliveira, P. (2016). Extreme mantle uplift
503   and exhumation along a transpressive transform fault. *Nature Geoscience*, *9*(8), 619-623.
504   https://doi.org/10.1038/ngeo2759
505
506   Melson, W. G., Jarosewich, E., Bowen, V. T., & Thompson, G. (1967). St. Peter and St. Paul Rocks: a high-
507   temperature, mantle-derived intrusion. *Science*, *155*(3769), 1532-1535.
508   https://doi.org/10.1126/science.155.3769.1532
509
510   Morgan, J. P., & Forsyth, D. W. (1988). Three-dimensional flow and temperature perturbations due to a transform
511   offset: Effects on oceanic crustal and upper mantle structure. *Journal of Geophysical Research: Solid
512   Earth*, *93*(B4), 2955-2966. https://doi.org/10.1029/JB093iB04p02955
513
514   Pan, J., & Dziewonski, A. M. (2005). Comparison of mid-oceanic earthquake epicentral differences of travel time,
515   centroid locations, and those determined by autonomous underwater hydrophone arrays. *Journal of Geophysical
516   Research: Solid Earth*, *110*(B7). https://doi.org/10.1029/2003JB002785
517
518   Prigent, C., Warren, J. M., Kohli, A. H., & Teyssier, C. (2020). Fracture-mediated deep seawater flow and mantle
519   hydration on oceanic transform faults. *Earth and Planetary Science Letters*, *532*, 115988.
520   https://doi.org/10.1016/j.epsl.2019.115988
521
522   Ren, Y., Lange, D., & Grevemeyer, I. (2023). Seismotectonics of the Blanco transform fault system, northeast
523   Pacific: Evidence for an immature plate boundary. *Journal of Geophysical Research: Solid Earth*, *128*(3),
524   e2022JB026045. https://doi.org/10.1029/2022JB026045
525   Roland, E., Behn, M. D., & Hirth, G. (2010). Thermal-mechanical behavior of oceanic transform faults:
526   Implications for the spatial distribution of seismicity. *Geochemistry, Geophysics, Geosystems*, *11*(7).
527   https://doi.org/10.1029/2010GC003034
528

529 Romanowicz, B., Cara, M., Fel, J. F., & Rouland, D. (1984). GEOSCOPE: A French initiative in long-period three-
530 component global seismic networks. *Eos, Transactions American Geophysical Union*, *65*(42), 753-753.
531 https://doi.org/10.1029/EO065i042p00753-01
532
533 Ryan, W. B., Carbotte, S. M., Coplan, J. O., O'Hara, S., Melkonian, A., Arko, R., ... & Zemsky, R. (2009). Global
534 multi-resolution topography synthesis. *Geochemistry, Geophysics, Geosystems*, *10*(3).
535 https://doi.org/10.1029/2008GC002332
536
537 Schilling, J. G., Ruppel, C., Davis, A. N., McCully, B., Tighe, S. A., Kingsley, R. H., & Lin, J. (1995). Thermal
538 structure of the mantle beneath the equatorial Mid-Atlantic Ridge: Inferences from the spatial variation of dredged
539 basalt glass compositions. *Journal of Geophysical Research: Solid Earth*, *100*(B6), 10057-10076.
540 https://doi.org/10.1029/95JB00668
541
542 Schlaphorst, D., Rychert, C. A., Harmon, N., Hicks, S. P., Bogiatzis, P., Kendall, J. M., & Abercrombie, R. E.
543 (2023). Local seismicity around the Chain Transform Fault at the Mid-Atlantic Ridge from OBS
544 observations. *Geophysical Journal International*, *234*(2), 1111-1124. https://doi.org/10.1093/gji/ggad124
545
546 Shi, P., Wei, M., & Pockalny, R. A. (2022). The ubiquitous creeping segments on oceanic transform
547 faults. *Geology*, *50*(2), 199-204. https://doi.org/10.1130/G49562.1
548
549 Sokos, E. N., & Zahradnik, J. (2008). ISOLA a Fortran code and a Matlab GUI to perform multiple-point source
550 inversion of seismic data. *Computers & Geosciences*, *34*(8), 967-977. https://doi.org/10.1016/j.cageo.2007.07.005
551
552 Turcotte, D., & Schubert, G. (2014). *Geodynamics* (3rd ed.). Cambridge: Cambridge University Press.
553 https://doi.org/10.1017/CBO9780511843877
554
555 The MathWorks Inc. (2019). MATLAB version: 9.6 (R2019a) [Software]. The MathWorks Inc.
556 https://www.mathworks.com
557
558 Vincent, C., Maia, M., Briais, A., Brunelli, D., Ligi, M., & Sichel, S. (2023). Evolution of a Cold Intra-Transform
559 Ridge Segment Through Oceanic Core Complex Splitting and Mantle Exhumation, St. Paul Transform System,
560 Equatorial Atlantic. *Geochemistry, Geophysics, Geosystems*, *24*(5), e2023GC010870.
561 https://doi.org/10.1029/2023GC010870
562
563 Wessel, P., Luis, J. F., Uieda, L. A., Scharroo, R., Wobbe, F., Smith, W. H., & Tian, D. (2019). The generic
564 mapping tools version 6. *Geochemistry, Geophysics, Geosystems*, *20*(11), 5556-5564.
565 https://doi.org/10.1029/2019GC008515
566
567 Wolfe, C. J., Bergman, E. A., & Solomon, S. C. (1993). Oceanic transform earthquakes with unusual mechanisms
568 or locations: relation to fault geometry and state of stress in the adjacent lithosphere. *Journal of Geophysical
569 Research: Solid Earth*, *98*(B9), 16187-16211. https://doi.org/10.1029/93JB00887
570
571 Zahradník, J., & Sokos, E. (2018). ISOLA code for multiple-point source modeling. *Moment tensor solutions: A
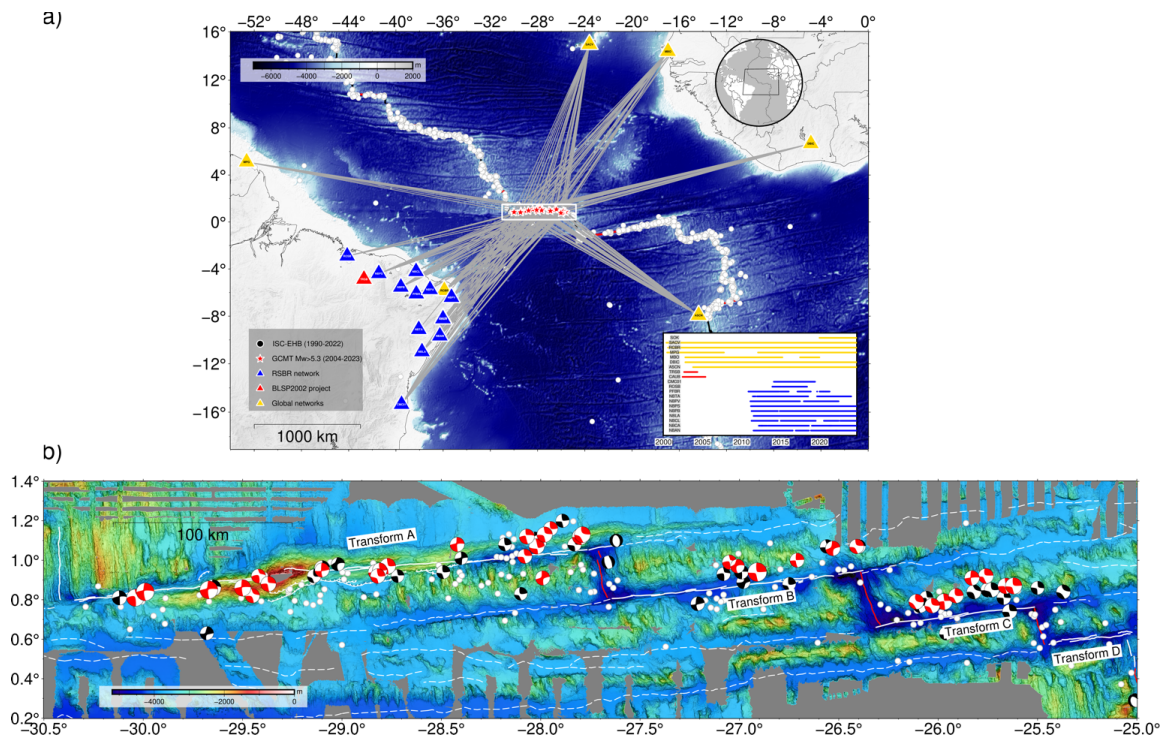572 useful tool for seismotectonics*, 1-28. https://doi.org/10.1007/978-3-319-77359-9_1
573

574

575
576 Figure 1: a) Regional bathymetric map of the equatorial Atlantic. Oceanic transform faults are presented by red lines,
577 while the mid-ocean ridges are shown in black lines (Sautter et al. 2024). White square refers to the Saint Paul
578 Transform System (SPTS, *Maia et al.* 2016). White circles represent the epicentral catalog of the International
579 Seismological Centre between 1990 and 2025 (Weston et al, 2018). Red stars indicate the earthquakes of the Global
580 Center Moment Tensor (GCMT) catalog with Mw>5.3, used in the surface waveform model. The modeling was done
581 using land and island stations of the Brazilian Seismographic network (RSBR, blue triangles, *Bianchi et al.* 2018),
582 global stations of the Incorporated Research Institutions for Seismology network (IRIS/IDA, Scripps Institution of
583 Oceanography, 1986), and GEOSCOPE networks (doi:10.18715/GEOSCOPE.G) presented by the yellow triangles,
584 and temporary land stations installed by the BLSP2002 project (*Feng et al.* 2004, red triangles). The histogram
585 showing the data availability of each station is shown on the right-hand side of the map. Gray lines represent the
586 source-station ray paths of the GCMT earthquakes used in focal depth analysis. b) Bathymetric map of the St. Paul
587 Transform System. Earthquakes with Mw>5.3 occurred since 1990 cataloged by the GCMT are shown in black
588 beachballs, with the events used in this study are presented by the red beachballs. White lines refer to the transform
589 fault segments along the SPTS, while the red lines refer to the intra-transform ridge axis (Maia et al. 2016). The
590 continuous white dashed lines refer to the fracture zones.
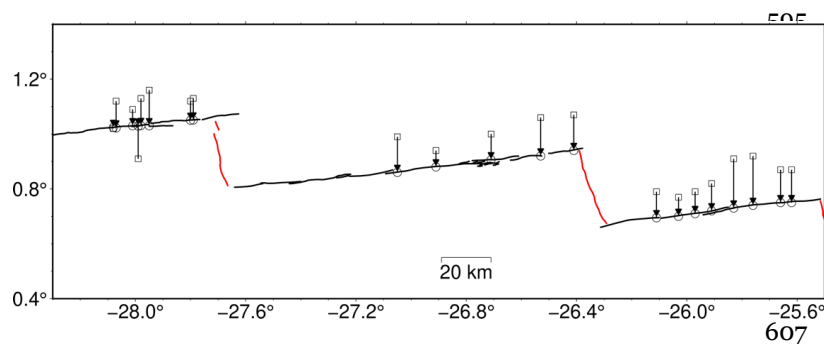591
592
593
594

17

Figure 2: Map of the moved epicenters. Black lines show the transform fault, while the intra-transform ridges are shown in red lines (Maia et al. 2016). Squares are the initial GCMT epicenter, with the moved location used on the waveform model presented by the circle symbols. The arrows connect the GCMT locations to the final locations, with a mislocation average of 11.25 km away.
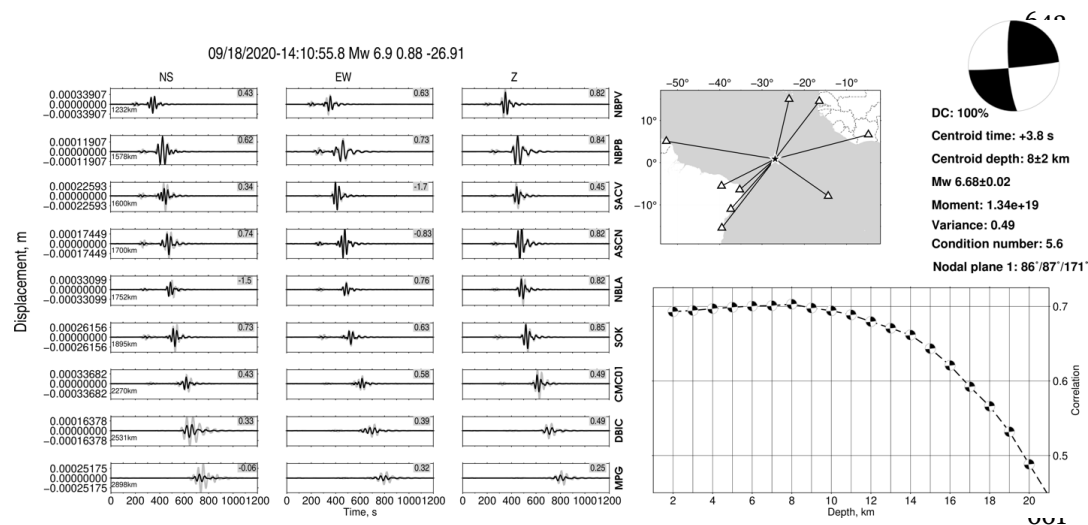
Figure 3: Focal depth analysis in SPTS of the Mw 6.9 earthquake occurred at Transform B in 09/18/2020. Left figure: Waveforms (gray) and their models (black) obtained with the best-fitting source position at 8 km depth. Middle upper figure: epicentral location map with their specified source-data ray paths for the respective seismic stations used on ISOLA analysis. Downright figure: Correlation vs Depth for the earthquake. The best solutions referent to each of the two earthquakes were fitted with higher correlation at 8±2 km depth.
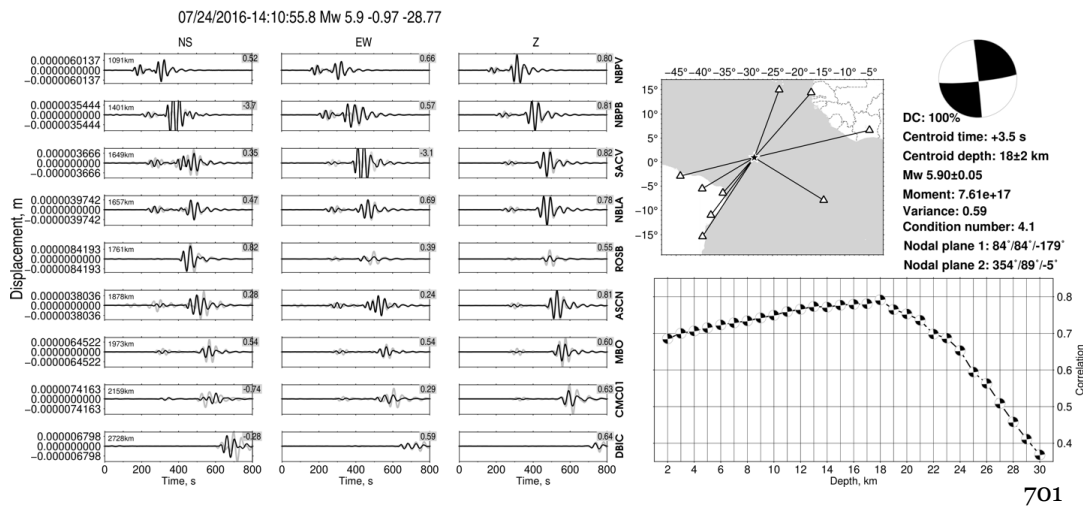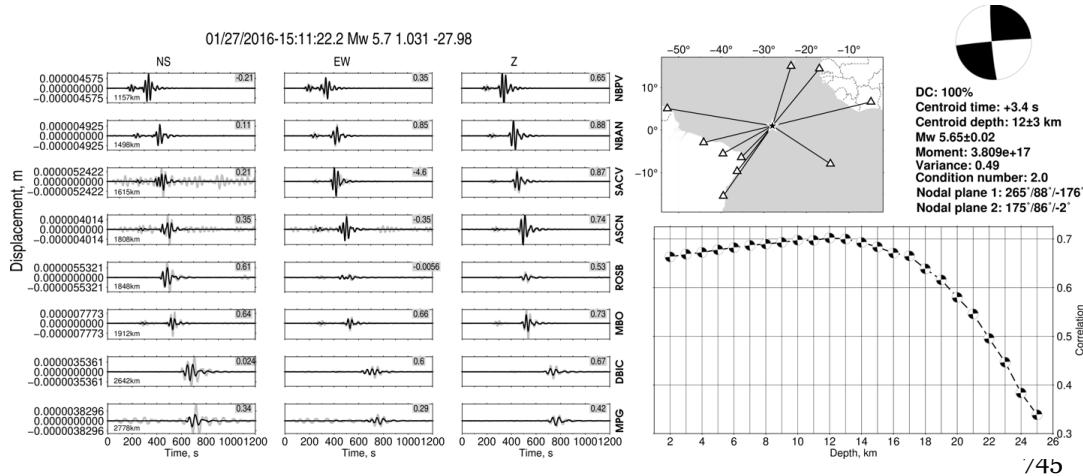
Figure 4: Focal depth analysis in SPTS of the Mw 5.9 earthquake occurred at Transform A in 07/24/2016. Left figure: Waveforms (gray) and their models (black) obtained with the best-fitting source position at 18 km depth. Middle upper figure: epicentral location map with their specified source-data ray paths for the respective seismic stations used on ISOLA analysis. Downright figure: Correlation vs Depth for the earthquake. The best solutions referent to each of the two earthquakes were fitted with higher correlation at 18±2 km depth.
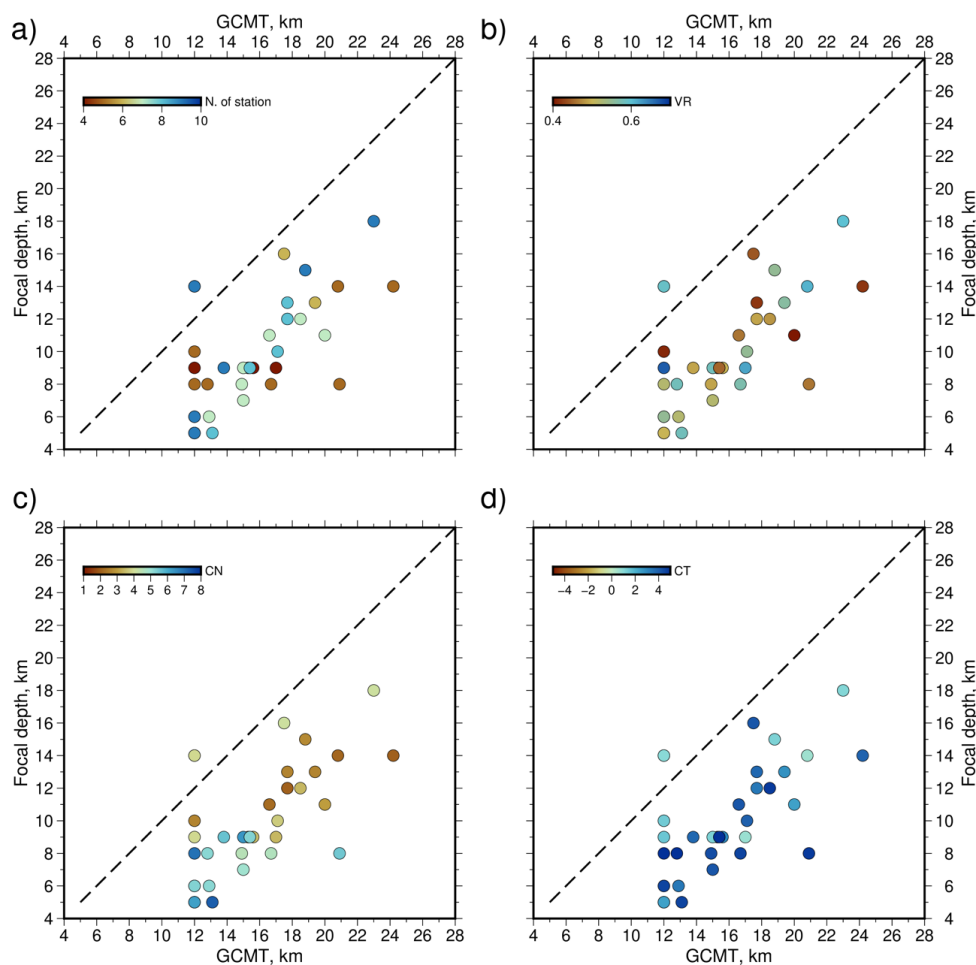
Figure 5: Focal depth analysis in SPTS of the Mw 5.7 earthquake occurred at Transform A in 01/27/2016. Left figure: Waveforms (gray) and their models (black) obtained with the best-fitting source position at 12 km depth. Middle upper figure: epicentral location map with their specified source-data ray paths for the respective seismic stations used on ISOLA analysis. Downright figure: Correlation vs Depth for the earthquake. The best solutions referent to each of the two earthquakes were fitted with higher correlation at 12±3 km depth.

Figure 6: Comparison of the focal depth analyzed in SPTS using regional records versus GCMT depth. The a) Comparison with the number of stations used in the analysis, presented by the symbol colors. Most of the earthquake had a minimum of six stations used in analysis, with most of the solutions presenting a synthetic/real waveform fitting with VR>0.5 (b). c) Symbol color showing the variation of the condition number (CN) of the ISOLA solution referent to each earthquake. Most solutions had CN<5. d) Comparison with the centroid-time (CT) obtained in waveform fitting, with most events presenting CT>0, indicating the existence of a difference between the origin time of the moment tensor solutions of the GCMT with the CT obtained using the regional stations.
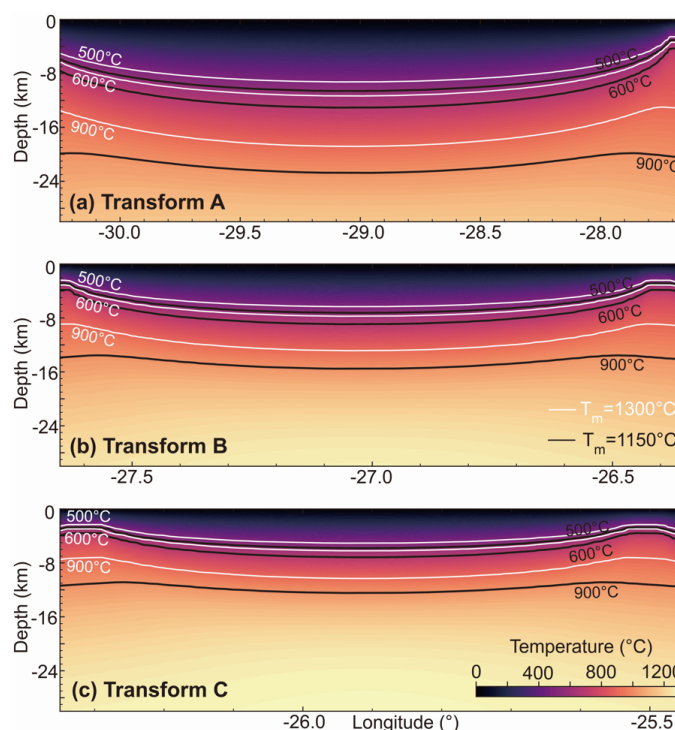
Figure 7: Half-space cooling model (HSCM) referent to Transform A, B, and C (a/b/c). Black lines refer to the model calculated assuming a mantle temperature of 1150ºC, referent to the respective maximum serpentinization depth at transform segments (500ºC, Maia et al 2016); the 600ºC referent to the expected maximum brittle-ductile transition (Abercrombie and Ekström 2001); and the limitation of the deep fluid-rock interaction with influence in deformation expected to occur until 900ºC (Prigent et al. 2020; Bickert et al. 2023). White lines indicate the results obtained for the same isotherms, but assuming the 1300ºC mantle temperature on HSCM. Due to the long-offset difference between the three transform segments, we can observe a considerable variation between the depth of the isotherms.
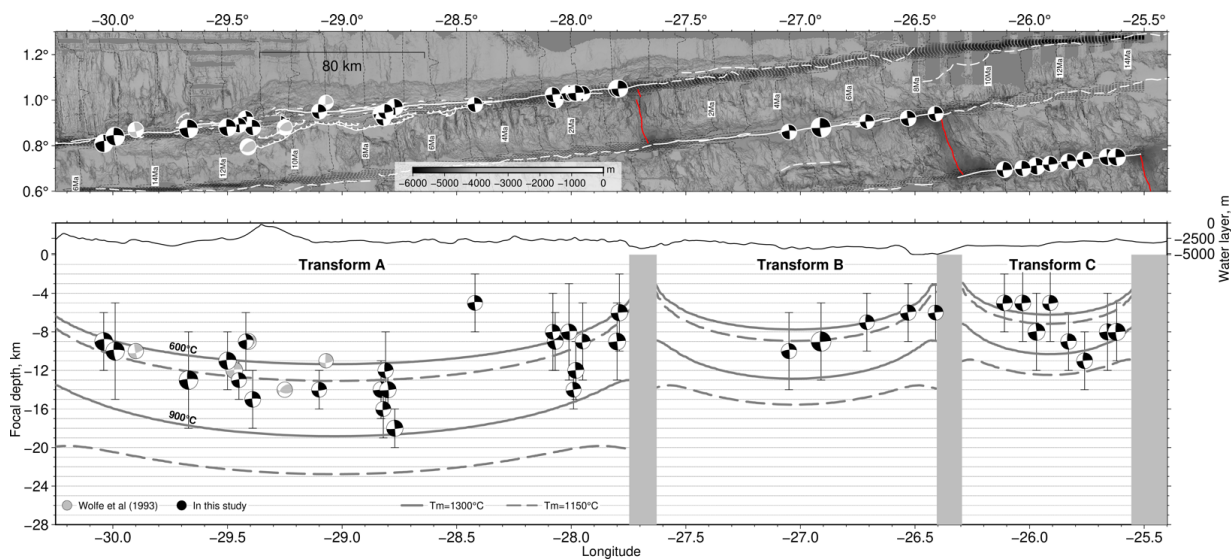
Figure 8: Earthquake focal depth distribution along the St. Paul transform system. Upper panel: Bathymetric map of the transform segments A, B, C. White lines refer to the transform faults, while red lines show the mid-ocean ridges tectonic plate boundaries mapped by Maia et al (2016). White dashed lines indicate the fracture zones. Black dashed lines show the crustal age variation in the St. Paul transform system (see Figure XX), calculated by Maia et al (2016). The epicenter locations of the 32 events of the GCMT catalog with Mw>5.3 are presented by the black beachballs. Gray beach balls refer to the earthquakes reported by Wolfe et al (1993) with a magnitude of 5.1<mb<5.9 (5.2<Mw<6.0; Kim et al. 2024). Bottom panel: cross-section of the Transform A, B, and C segments following the map longitude range, with the vertical distribution of the 32 earthquakes analyzed in this study (black beachballs) and the five earthquakes reported by Wolfe et al (1993). Vertical uncertainties of the focal depths varying from 2 to 5 km are presented by the thinner vertical black lines. The gray isotherms lines indicate the thermal structure for temperatures of 600, and 900°C beneath the SPTS assuming the mantle temperature of 1300°C, while the dashed gray lines refer to the mantle temperature of 1150°C. In both two models, at least 18 earthquakes are located at depths deeper than the 600°C isotherm, the predicted brittle-ductile transition beneath the oceanic transform faults (Abercrombie and Ekstrom. 2001).
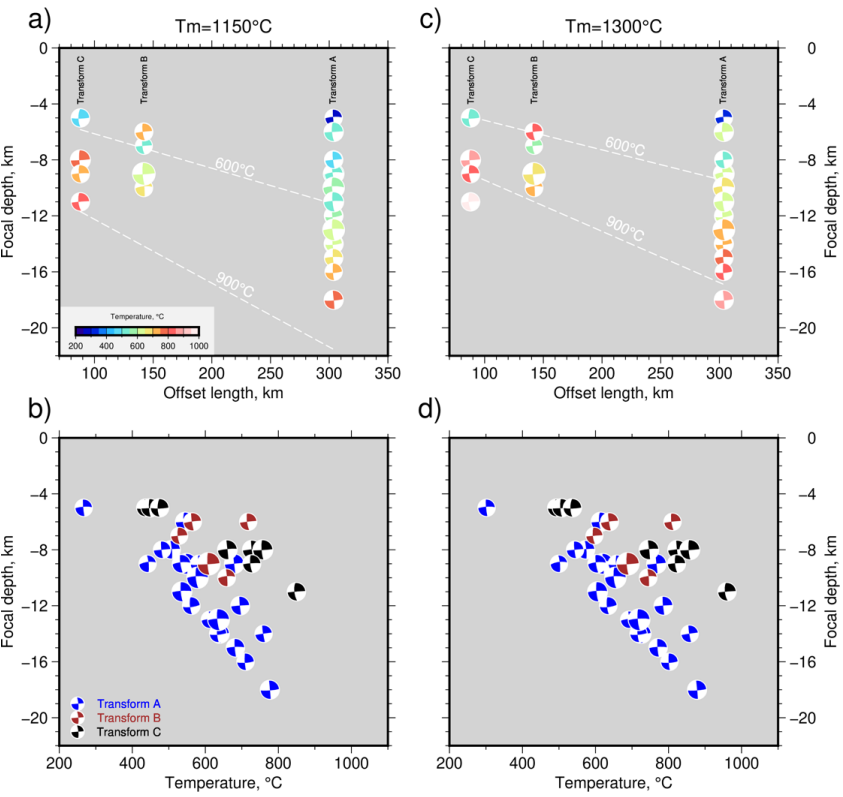
Figure 9: a/b Comparison of the focal depth with the offset length of the Transform A, B, C (Ren et al 2021) and calculated temperatures, respectively. A mantle temperature of 1150°C was assumed for results presented in both a/b. Results obtained using a hotter mantle temperature of 1300°C is shown in c/d. We can observe a gradual increase of the maximum focal depth with the increase of the offset length, which is expected to occur along the half-space cooling.